Mathematical Biosciences 351 (2022) 108883

Contents lists available at ScienceDirect

Mathematical Biosciences

journal homepage: www.elsevier.com/locate/mbs

Original Research Article

Entrainment within hierarchical circadian oscillator networks

Guangyuan Liao [a], Amitabha Bose [b,*]

[a] Key Laboratory of Intelligent Analysis and Decision on Complex Systems, School of Science, Chongqing University of Posts and Telecommunications, Chongwen Road, Nan'an, 400065, Chongqing, China

[b] Department of Mathematical Sciences, NJIT, Newark, NJ, 07102, USA

ARTICLE INFO

Keywords:
Circadian rhythms
Entrainment
Stable and unstable manifolds
Poincaré map

ABSTRACT

Circadian rhythms are endogenous oscillations, widely found across biological species, that have the capability of entraining to the 24-h light-dark cycle. Circadian systems often consist of both central oscillators that receive direct light-dark input and peripheral oscillators that receive input from the central oscillators. In this paper, we address questions related to what governs the time to and pattern of entrainment of these hierarchical circadian systems after an abrupt switch in the light-dark phasing. For a network consisting of a single central oscillator coupled to a chain of N feed-forward peripheral oscillators, we introduce a systematic way to derive an N-dimensional entrainment map whose fixed points correspond to entrained solutions. Using the map, we explain that the direction of reentrainment can involve fairly complicated phase advancing and delaying behavior as well as reentrainment times that depend sensitively on the nature of the perturbation. We also study the dynamics of a hierarchical system in which the peripheral oscillators are mutually coupled. We study how reentrainment times vary as a function of the degree to which the oscillators are desynchronized at the time of the change in light-dark phasing. We show that desynchronizing the peripheral oscillators can, in some circumstances, speed up their ultimate reentrainment following perturbations.

1. Introduction

Circadian oscillations provide a natural, nearly 24 h clock to many living systems. For humans this is characterized by our response to the 24 h light-dark cycles of the sun and helps regulate many of our functions such as our sleep-wake cycles. Hormone levels, such as melatonin, are also governed by circadian rhythms. Plants, bacterias and animals also possess circadian rhythms. In all of these cases, the oscillators in control of these rhythms are meant to entrain to the 24 h light-dark (LD) cycle to ensure proper functioning of the organism. Often these oscillators are peripheral and do not directly receive light-dark input from the sun. Instead, they receive forcing from a central set of oscillators that do directly receive the light-dark input. The ensuing network architecture of central oscillators receiving light-dark forcing, with peripheral oscillators receiving input from the central oscillators constitutes a hierarchical coupled set of oscillators.

Hierarchical circadian systems are known to exist in non-mammalian systems such as *Neurospora crass* as well as in several mammalian systems [1]. Within humans, for example, the suprachiasmatic nucleus (SCN) has been identified as the master pacemaker and its neurons have been classified into two groups: ventral SCN neurons which receive direct light input and dorsal SCN neurons that do not [2]. Ventral SCN neurons provide timing information to dorsal neurons. As a hierarchical unit, these two groups synchronize to provide timing information to the rest of the body. A second way in which mammalian systems constitute a hierarchical system involves the observation that various organ systems possess cells that have their own endogenous circadian clocks. Cells in peripheral organs such as the heart, lungs and kidney do not need light input to oscillate [1], but do receive entraining timing information from the central SCN pacemaker unit. Some peripheral units, such as the liver, may also receive other timing inputs through rhythmic feeding cues [3], which has been argued as a source for possible desynchronization of central and peripheral clocks [4]. Of interest in hierarchical networks is not just the phase-locking of oscillators at different hierarchical levels, but also the synchronization and phase-locking properties of oscillators within the same level of hierarchy.

Given any circadian oscillator, there are a few basic questions to be addressed. First, what kinds of external (*zeitgeber*) input entrain the oscillator? When an oscillator is perturbed from the entrained state, how long does it take to reentrain? Is the direction of reentrainment through phase advance, delay or some combination with respect to the external input? These questions become more challenging to address in hierarchical systems where distinct circadian components can display very different dynamics after perturbations. For example, Leise and Siegelmann [5] conducted a numerical study of a multi-stage network in which they found that after changes in the LD phasing to the

* Corresponding author.
E-mail address: bose@njit.edu (A. Bose).

https://doi.org/10.1016/j.mbs.2022.108883
Received 13 December 2021; Received in revised form 15 July 2022; Accepted 18 July 2022
Available online 27 July 2022

network, peripheral and central oscillators can have different times and directions of entrainment. They call this phenomenon where some oscillators reentrain through phase advance and others through phase delay, reentraiment by partition, which they suggest can lead to longer reentrainment times. Abraham et al. [6] found similar results with regard to entrainment time in a modeling and experimental study involving circadian clocks in the central suprachasmatic nucleus and in peripheral clocks of the lung. Often the difference in the reentrainment process is attributed to central oscillators displaying strong, large amplitude oscillations, which had been thought to slow the reentrainment, compared to peripheral oscillators. Recently however, Jeong et al. [7] found that some strong central oscillators can under some circumstances also display fast reentrainment after a shift in light-dark phasing. Modeling studies of jetlag and shift work [8–11] have also found that different amplitudes of oscillation lead to different entrainment times, though in those studies smaller amplitude led to faster entrainment.

Among the many existing tools to study the entrainment of oscillators [12–14], we will primarily utilize the entrainment map developed by Diekman and Bose [15]. Originally developed to study entrainment of a single circadian oscillator, in Liao et al. [16], we generalized the map to apply to the case of one central and one peripheral oscillator, both modeled by the two-dimensional Novak–Tyson oscillators [17]. Here we are interested in understanding the dynamics of reentrainment in networks of one-dimensional phase models. Simplified lower-dimensional phase models such as the Poincaré oscillator [18] or Kuramoto model [18] have been used to study circadian oscillations in a variety of contexts [8,19,20]. In particular, Bordyugov et al. [20] showed that the findings from these reduced models often matches that of higher dimensional biochemical models. Further, use of low-dimensional models allows for application of a host of analytic and computational tools to better understand the nature of entrainment.

In this paper, we consider two different types of hierarchical systems and derive entrainment maps to study their dynamics. For a system of $1+N$ oscillators (the first oscillator represents the 24 h external light-dark forcing) coupled together in a feed-forward manner, we derive an N-dimensional entrainment map and study it in detail for the case $N=2$. We show how to use geometric structures of the phase space, such as invariant manifolds of fixed points, to determine the time to and direction of reentrainment of oscillators within the coupled system after an abrupt change (slam shift) in the LD phase, a desynchronization of the central and peripheral oscillator, or both. We then generalize to the larger $1+N$ dimensional system where we show that the existence and stability of fixed points of the entrainment map can be predicted from the previous level of the hierarchy.

A second kind of hierarchical system we shall consider consists of a pair of coupled peripheral oscillators receiving input from a single central oscillator. We will use an order parameter description for the peripheral oscillators to derive a two-dimensional entrainment map involving their average phase. We study how the reentrainment time after an abrupt switch in the light-dark phase is affected by the degree to which the peripheral oscillators are desynchronized, or phase tumbled [21–24], at the time of the switch of light phasing. We find that when the peripheral oscillators have entrained solutions in which their phase difference is small, they do not exhibit much difference in reentrainment time for different initial levels of desynchrony. However, when the peripheral oscillators in the entrained solution exhibit a larger phase difference, then further initial desynchrony can speed up the reentrainment process for certain, but not all, abrupt changes in the light-dark phasing.

2. Model

In the first part of our study, we shall consider a system of $1+N$ oscillators. The first, defined by the variable θ_0, is a simple time keeper for the 24 h light-dark (LD) cycle. The other N oscillators are taken from the Kuramoto model [18] and described by their phase. Each of these oscillators has its own intrinsic frequency. They are coupled together through sine function interactions based on the differences in their phases arranged in a hierarchical structure. Namely, oscillator 1 receives input from the LD oscillator θ_0. Oscillator n receives input from oscillator $n-1$. The equations that define the model are:

$$\begin{aligned}\frac{d\theta_0}{dt} &= \omega_0\\ \frac{d\theta_1}{dt} &= \omega_1 + k f(\theta_0)\sin(\theta_0-\theta_1)\\ \frac{d\theta_i}{dt} &= \omega_i + \alpha_{i-1}\sin(\theta_{i-1}-\theta_i)\ i=2,\dots,N\end{aligned} \tag{1}$$

The frequency of the light-dark forcing is $\omega_0 = 2\pi/24$ since the period of one day is $T=24$. The intrinsic frequencies ω_i are taken to lie in a neighborhood of ω_0 and need not be the same. Each of these phase variables can be viewed as taking on values either on the real line or restricted to any 2π interval. We will interchangeably use both interpretations depending on the context. We will study how solutions depend on the parameters k, the strength of the light-dark forcing to θ_1, and α_{i-1}, the strength of the forcing from θ_{i-1} to θ_i. The function $f(\theta) = Heaviside(\sin(\theta))$, is 0 when $\sin\theta<0$ and 1 otherwise. The abrupt on-off nature of light input due to the Heaviside function is a simplification for the continuous change under more natural circumstances. However, this abrupt switch is used in many experimental protocols e.g. [25] and modeling studies e.g. [26] and is referred to as a "slam shift".

To define the entrainment map, we fix an N-dimensional global section $\mathcal{P} = \{(\theta_0,\theta_1,\dots,\theta_N) : \theta_N = \pi\}$ of the flow of (1); see Fig. 1 for a schematic of the simplest case of $N=2$). On this section, $\theta_N=\pi$, thus leaving the θ_0 and θ_i, $i=1,\dots,N-1$ values to be determined. On the Poincaré section $\mathcal{P}$, we define $x=\theta_0$, $y=\theta_1$ and $z_i=\theta_i$, $i=2\dots N-1$. Starting with a point on the section, flow forward in time until the trajectory returns to $\mathcal{P}$ and denote this time as $\rho=\rho(v)$, where $v=(x,y,z,k,\alpha)$, $z=(z_2,\dots,z_{N-1})$ and $\alpha=(\alpha_1,\dots,\alpha_{N-1})$. Note that this time measures how long it takes oscillator N to complete one 2π cycle and is obtained by integrating the third equation of (1) with $i=N$. The new phases of x of the LD cycle, of y and z of oscillators 1 to $N-1$ are obtained by integrating (1) from 0 to the return time ρ and performing a mod 2π operation. Therefore the N-dimensional entrainment map is defined by:

$$\begin{aligned}x &\mapsto F_1(x,y,x,k,\alpha) := x+\omega_0\rho \bmod 2\pi\\ y &\mapsto F_2(x,y,z,k,\alpha) := y+\omega_1\rho + kI_1 \bmod 2\pi\\ z_i &\mapsto F_{i+1}(x,y,z,k,\alpha) := z_i+\omega_i\rho+\alpha_{i-1}I_i \bmod 2\pi\end{aligned} \tag{2}$$

where $I_1 = \int_0^\rho f(\theta_0)\sin\left(\theta_0-\theta_1\right)dt$ and $I_i = \int_0^\rho \sin\left(\theta_{i-1}-\theta_i\right)dt$, $i=2,\dots,N-1$. Because of the mod operation in both variables and periodicity, the phase space is actually a torus $S_1\times\cdots\times S_1$. When we focus on the case of $N=2$, we will visualize this phase space on the square where the edges $x=0$ and $x=2\pi$ are identical as are the edges $y=0$ and $y=2\pi$.

A fixed point (x^*,y^*,z^*) of the entrainment map corresponds to a periodic phase locked solution of the system (1). The value x^* determines the phase of lights when oscillator N is at $\mathcal{P}$. We are assuming that the LD cycle is broken up into 12 h of light, $\theta_0\in(0,\pi)$ and 12 h of darkness, $\theta_0\in(\pi,2\pi)$. Thus the value x^* means that the most recent light onset occurred $12x^*/\pi$ hours ago. There is no difficulty in considering other photoperiods with less or more hours of light per day. The value y^* yields the phase of oscillator 1 at the fixed point, where $y^*-\pi\in(-\pi,\pi)$ can be interpreted as the phase difference from oscillator N and similarly for the oscillators corresponding to z^*. Note that since the evolution of each θ_i is not constant, the phase difference may vary over the length of one cycle before returning to the original difference once oscillator N returns to $\mathcal{P}$. We will show that the entrainment map can possess from 0 to 2^N fixed points depending on the choice of parameters k and α_i. Using standard linearization techniques we assess the stability of these fixed points to show how their manifolds

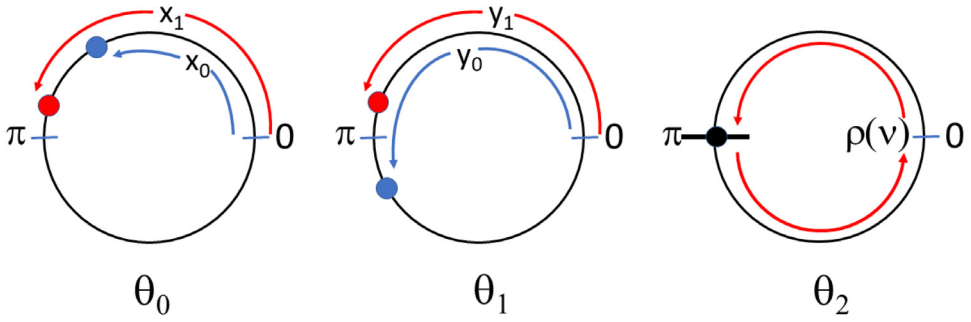

Fig. 1. Schematic defining terms for the $N = 2$ entrainment map. The direction of flow is counterclockwise for all cases. The Poincaré section at $\theta_2 = \pi$, shown with a dark solid line, is where oscillator 2 initially lies (black solid dot). The blue solid dots on θ_0 and θ_1 denote the initial locations of the LD oscillator and oscillator 1, respectively. The corresponding initial values for the map are given by x_0 and y_0. Oscillator 2 takes $\rho(v)$ time to complete one cycle and return to the Poincaré section. For illustration we assume that this time is larger than 24 h. The red dots depict the locations of the LD oscillator and oscillator 1 after $\rho(v)$ hours. Note that the time for θ_0 to complete one cycle is 24 h. Thus the value $x_1 > x_0$. The cycle time of oscillator 1, however, is *a priori* not known, meaning that the location of y_1 is also not known. We have chosen to schematically depict it as $y_1 < y_0$. The map takes the initial values x_0 and y_0 and returns the new values x_1 and y_1.

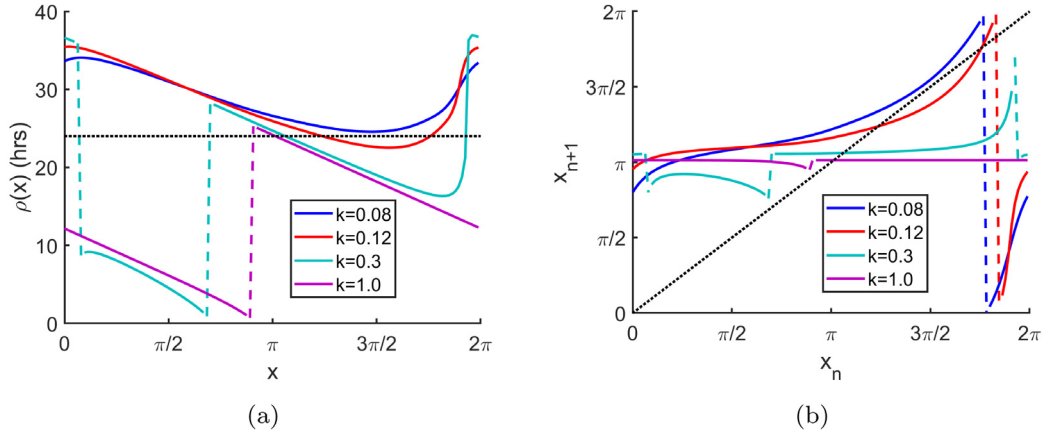

Fig. 2. The return time and entrainment maps with different k values. (a) The 1-dimensional return time map plots with five different k values. When k is large, the return time function $\rho(x)$ becomes discontinuous. (b) The 1-dimensional entrainment map plots for the same k values. As k increases from small values, fixed points are gained through a saddle node bifurcation. As k increases further, the map loses one fixed point through the discontinuity associated with $\rho(x)$.

organize the iterate structure of the map. Corresponding to the stable and unstable fixed points of the map, there exists both stable and unstable periodic solutions of Eq. (1). Each of these types of periodic solutions are actually phase-locked solutions of the light-dark forcing. We shall refer to the stable ones as entrained solutions and the unstable ones as solutions in an unstable state.

In the second part of our study, we will consider a $1 + N$ network with $N = 3$, in which the two peripheral oscillators are mutually coupled to one another. The equations for this system are given by:

$$\begin{aligned}
\frac{d\theta_0}{dt} &= \omega_0 \\
\frac{d\theta_1}{dt} &= \omega_1 + kf(\theta_0)\sin(\theta_0 - \theta_1) \\
\frac{d\theta_2}{dt} &= \omega_2 + \alpha_1 \sin(\theta_1 - \theta_2) + \alpha_3 \sin(\theta_3 - \theta_2) \\
\frac{d\theta_3}{dt} &= \omega_3 + \alpha_1 \sin(\theta_1 - \theta_3) + \alpha_2 \sin(\theta_2 - \theta_3)
\end{aligned} \tag{3}$$

The values of parameters are $\omega_0 = \frac{2\pi}{24}, \omega_1 = \frac{2\pi}{27}, \omega_2 = \frac{2\pi+1}{29}, \omega_3 = \frac{2\pi-1}{29}, k = 0.08, \alpha = 0.1, \alpha_2 = \alpha_3 = 0.3$. Note here that we choose the intrinsic frequencies of the peripheral oscillators to differ. In the results, we will show how this heterogeneity can contribute to speeding up the reentrainment process. To build the entrainment map, we now choose the Poincaré section using the central oscillator at $\theta_1 = \pi$.

3. Results

3.1. 1-Dimensional entrainment maps

Consider the case of the LD forcing with strength k acting on oscillator 1. Here we are taking $\alpha_1 = 0$ (consider only the first two equations of (1)). We place the Poincaré section at $\theta_1 = \pi$ and compute the return time $\rho = \rho(x)$. The 1-dimensional entrainment map is then simply given by the first equation of (2). In Fig. 2(a), we show the return time $\rho(x)$ for several values of the strength k of the LD forcing. Panel (b) shows the entrainment map for these same values. Both the return time and the entrainment map are periodic in that their values at the boundaries $x = 0$ and $x = 2\pi$ are the same. For $k = 0.08$, the coupling from the LD forcing is not strong enough to entrain oscillator one. The return time is always larger than 24 h and the entrainment map does not intersect the diagonal (blue curves in Fig. 2a, b). Note that while the return time is continuous at this value, the entrainment map has a discontinuity due to the mod 24 operation. As k increases, the entrainment map shifts down and two fixed points (red curves) are

created through a saddle-node bifurcation at roughly $k = 0.09$. The exact value will be labeled in the section below as k_c. With a further increase in k, the return time map becomes discontinuous (green curve) at two values for $x < \pi$. The entrainment map shares discontinuities at those points, but the discontinuity due to the mod is replaced by a different type of discontinuity which will be discussed below. As k increases further the map begins to flatten out near the value π for larger parts of the domain, while the discontinuity shifts to the right. At $k = 1$, the entrainment map is nearly horizontal with a single fixed point at $x = \pi$. The flattening out of the map makes sense since as the LD forcing becomes stronger, almost all initial conditions quickly get entrained to the LD forcing and the values of θ_0 and θ_1 become identical. Since the x value of the map is the value of θ_0 and the map updates whenever $\theta_1 = \pi$, this implies that $x = \pi$.

To further explain the results for larger values of k consider a singular perturbation argument. Consider the single oscillator model

$$\begin{aligned} \frac{d\theta_0}{dt} &= \omega_0 \\ \frac{d\theta_1}{dt} &= \omega_1 + kf(\theta_0)\sin(\theta_0 - \theta_1). \end{aligned} \tag{4}$$

Let $\epsilon = 1/k, \tau = t/\epsilon$ to obtain

$$\begin{aligned} \frac{d\theta_0}{d\tau} &= \epsilon\omega_0 \\ \frac{d\theta_1}{d\tau} &= \epsilon\omega_1 + f(\theta_0)\sin(\theta_0 - \theta_1). \end{aligned} \tag{5}$$

Thus as $\epsilon \to 0$, on fast time scale, the system reduces to a 1-dimensional system

$$\begin{aligned} \frac{d\theta_0}{d\tau} &= 0 \\ \frac{d\theta_1}{d\tau} &= f(x_0)\sin(x_0 - \theta_1), \end{aligned} \tag{6}$$

where $x_0 = \theta_0(0)$. When $x_0 > \pi, f(x_0) = 0$, θ_1 is a constant and equals its initial condition. When $x_0 < \pi, f(x_0) = 1$,

$$\frac{d\theta_1}{d\tau} = \sin(x_0 - \theta_1). \tag{7}$$

The fixed points are $\theta_1 = x_0$ (stable) or $\theta_1 = x_0 + \pi$ (unstable). Given the choice of Poincaré section, the fast equation implies that solutions converge to the stable fixed point x_0.

By returning to the original time scale, we obtain

$$\begin{aligned} \frac{d\theta_0}{dt} &= \omega_0 \\ \epsilon\frac{d\theta_1}{dt} &= \epsilon\omega_1 + f(\theta_0)\sin(\theta_0 - \theta_1) \end{aligned} \tag{8}$$

which when $\epsilon = 0$ yields

$$\begin{aligned} \frac{d\theta_0}{dt} &= \omega_0 \\ 0 &= f(\theta_0)\sin(\theta_0 - \theta_1). \end{aligned} \tag{9}$$

On the original time scale, when $f(\theta_0) \neq 0$, it must follow that $\sin(\theta_0 - \theta_1) = 0$ implying that $\theta_0 = \theta_1$ remains. Thus when θ_1 returns to the Poincaré section again, $\theta_1 = \pi$ and therefore $x = \pi$ is the only fixed point. While this argument explains why there is only one fixed point in the limit $k \to \infty$, the map results shown in Fig. 2 indicate that this result holds at much smaller values of k.

We next add a second oscillator and consider a 1-dimensional map under the assumption that θ_1 is already entrained where $k = 0.1$. In Fig. 3, we obtain similar results as the previous 1-dimensional map. If α_1 is too small then θ_2 cannot be entrained. As α_1 increases from 0.04 to 0.08, a saddle node bifurcation occurs at an intermediate value that we will identify in the next section as α_c. As the value of α_1 continues to increase, a discontinuity arises and the unstable fixed point disappears. A similar singular perturbation argument as above with $\epsilon = 1/\alpha_1$ can be used to show this.

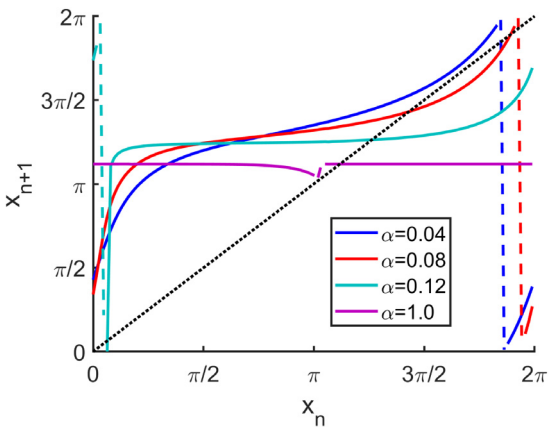

Fig. 3. The 1-dimensional map for the entrainment of θ_2 in which θ_1 is already entrained with different α_1 values. No fixed points exist for small values of α_1, two for intermediate values of α_1 and only the stable one when α_1 is large.

3.2. Necessary conditions for entrainment of two oscillators

Now let us turn our attention to the three oscillator case in which we allow both $k, \alpha_1 > 0$. Whether an entrained solution exists or not depends on parameters. Fig. 4 shows phase differences of θ_1 and θ_2 from θ_0 for a case of non-entrainment (a) and entrainment (b). In both panels, oscillator 1 is entrained to the LD oscillator as the coupling constant k is sufficiently large. In Fig. 4(a), the coupling from oscillator 1 to 2, α_1 is too small (the phase difference is not periodic), while in the other panel it is strong enough to yield entrainment. This simulation suggests, not surprisingly, that there exist a range of parameters over which entrained solutions exist.

Finding an entrained solution of (1) is equivalent to finding a stable fixed point of the entrainment map. From the first equation of (2), we need $F_1(x, y, k, \alpha) = x$, which implies $\rho(\theta_0, \theta_1) = 24$. From the second equation of (2) similarly, we need

$$24\omega_1 + k\int_0^{24} f(\theta_0)\sin\left(\theta_0 - \theta_1\right)dt = 2\pi. \tag{10}$$

Since $f(\theta_0) \leq 1$ and $|\sin(\theta_0 - \theta_1)| \leq 1$, the following bound for k is obtained

$$k \geq 2|\omega_0 - \omega_1|. \tag{11}$$

In other words k must be sufficiently larger than the difference between the intrinsic frequencies of the LD and first oscillator.

To obtain a bound for α_1, note that based on the definition of Poincare section, ρ also satisfies $\theta_2(\rho) = 3\pi$. Integrating the equation for θ_2 from 0 to ρ, we obtain:

$$2\pi = \omega_2\rho + \alpha_1\int_0^{\rho}\sin\left(\theta_1 - \theta_2\right)ds. \tag{12}$$

Substitute $\rho(\theta_0, \theta_1) = 24$ into (12) as a necessary conditions for the system to have an entrained solution to obtain:

$$\alpha_1 \geq \frac{|2\pi - 24\omega_2|}{24} = |\omega_0 - \omega_2| \tag{13}$$

Note that this bound does not specifically include the term ω_1. This occurs because the necessary condition for entrainment is that θ_1 is already entrained and thus oscillates with a 24 h period. Thus it is enough to compare the intrinsic frequency ω_2 to ω_0 and ensure that coupling strength α_1 from θ_1 is sufficiently large.

3.3. Existence and stability of fixed points of the 2-dimensional map

Knowing the necessary conditions for entrainment allows us to now turn to finding fixed points of the entrainment map. For the map to

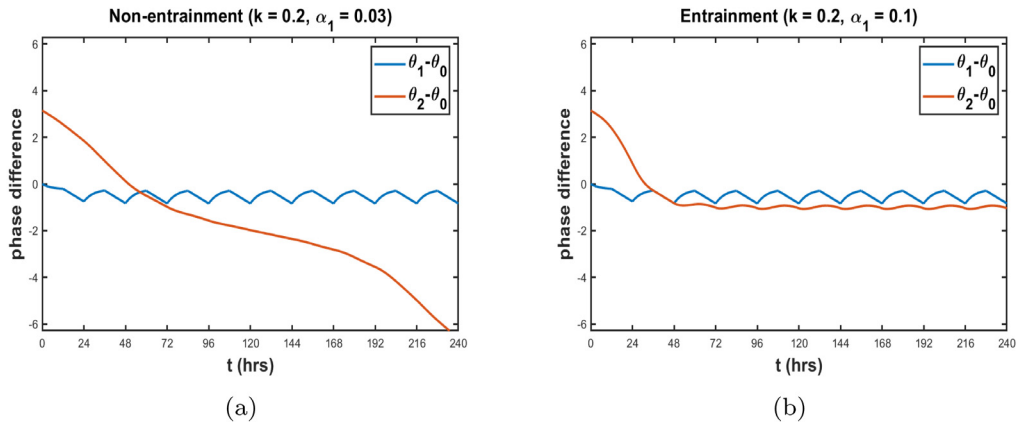

Fig. 4. The phase difference of the original system showing (a) non-entrainment and (b) entrainment. The blue curve denotes $\theta_1 - \theta_0$, and the red curve denotes $\theta_2 - \theta_0$. **(a)** The value of k is large enough to entrain θ_1 to θ_0, but α_1 is too small to entrain θ_2 to θ_1 as exemplified by the phase slipping of θ_2. **(b)** Both k and α_1 are sufficiently large for entrainment. The oscillators quickly come into alignment and remain entrained.

have fixed points, Eq. (2) implies that

$$\begin{aligned} F_1(x, y, k, \alpha_1) - x &= 0 \\ F_2(x, y, k, \alpha_1) - y &= 0. \end{aligned} \tag{14}$$

In the Appendix, we show that there exist $s_1, s_2 \in (0, 24)$ such that Eq. (14) is equivalent to

$$\begin{aligned} \sin\left(\theta_1(s_1) - \theta_2(s_1)\right) &= \frac{\omega_0 - \omega_2}{\alpha_1} \\ \sin\left(\theta_0(s_2) - \theta_1(s_2)\right) &= \frac{2(\omega_0 - \omega_1)}{k}. \end{aligned} \tag{15}$$

Notice that the absolute value of the left hand side of both equations is bounded by one which immediately allows us to recover the necessary conditions on parameters for entrainment, Eqs. (11) and (13). The left-hand sides of (15) are both 2π-periodic sine functions. The right-hand sides are just horizontal lines. Thus these lines each intersect the sin functions at most at two points in $[0, 2\pi)$. By choosing one intersection point from each of these graphs, we obtain four possible fixed points. We can also see why fixed points arise at small values of k or α_1. For example, when k increases, the horizontal line defining the right-hand side of the first equation in (15) decreases towards the value 1. Thus this equation can have at most one solution at the moment when the equation is first satisfied, followed by at most two solutions as k further increases. Define

$$\begin{aligned} k_c &= 2(\omega_0 - \omega_1) \\ \alpha_c &= \omega_0 - \omega_2. \end{aligned} \tag{16}$$

These are the critical values of k and α_1 that arise due the saddle-node bifurcations in the 1-dimensional maps discussed in Section 3.1. When $k < k_c$, θ_1 cannot be entrained by the light forcing; when $\alpha_1 < \alpha_c$, θ_2 cannot be entrained by θ_1. The nature of entrainment depends on the choice of the parameter pair (k, α_1). Specifically, there exist four curves in the parameter space that separate regions where there are four, two or one fixed point (Fig. 5a). Two of these curves are the lines $k = k_c$ and $\alpha = \alpha_c$. The other two curves are described below in Case I.

Case I: There exist curves $k_{ub}(\alpha_1)$ (Fig. 5(a) green) and $\alpha_{ub}(k)$ (Fig. 5(a) red) that together with the lines $k = k_c$ and $\alpha_1 = \alpha_c$ bound a region R in parameter space such that for any parameter pair chosen in the interior of R, the two-dimensional map has four fixed points. The subscript ub denotes the upper bound.

Case II: If $\alpha_1 < \alpha_{ub}(k)$ and $k > k_{ub}(\alpha)$, or if $\alpha_1 > \alpha_{ub}(k)$ and $k < k_{ub}(\alpha)$ then for any parameter pair chosen in either of those regions, the map possesses two fixed points.

Case III: Define $\alpha_d = \alpha_{ub}(k_c)$ and $k_d = k_{ub}(\alpha_c)$. If $k = k_c$, for $\alpha_c < \alpha_1 < \alpha_d$ there are two fixed points and for $\alpha_1 > \alpha_d$ there is one fixed point. Similarly, if $\alpha_1 = \alpha_c$, for $k_c < k < k_d$, there are two fixed points and for $k > k_d$, there is one fixed point.

Case IV: If $k > k_{ub}(\alpha)$ and $\alpha_1 > \alpha_{ub}(k)$, then the map possesses exactly one fixed point.

Fig. 5(b)–(e) shows bifurcation curves obtained by varying either k or α_1 along the lines labeled (b)–(e) in panel (a). Solid (dashed) curves denote curves of stable (unstable) fixed points. Focusing first on panel (b) where $k = 0.12$, one sees that at a small value of $\alpha_1 = \alpha_c$, two separate bifurcations occur leading to the creation of four fixed points. To understand this, return to the 1-dimensional maps considered in Section 3.1. With $k = 0.12$, Fig. 2 shows that the 1-dimensional entrainment map has two fixed points, a stable and an unstable one. Using the stable fixed point value of this map, we then see from Fig. 3 that when α_1 is too small, this 1-dimensional map has no fixed points. However, an increase of α_1 leads to the creation of two fixed points via a saddle-node bifurcation. This explains the creation of the green and purple curves of Fig. 5(b). The green curve corresponds to the situation where θ_1 is entrained to the LD oscillator θ_0 and θ_2 is entrained to θ_1. The purple curve corresponds to the case where θ_1 is entrained to the LD oscillator θ_0, but θ_2 is in an unstable state with respect to θ_1.

To understand why the set of blue and red bifurcation curves arise, use the unstable fixed point of the $\theta_0 - \theta_1$ map, repeating the same argument as above. Now we obtain the case where θ_1 is in an unstable state relative to θ_0, while θ_2 is either entrained (blue curve) or in an unstable state relative (red curve) to θ_1. Notice that the blue and purple curves switch their location in Fig. 5(b). This switch is caused by the mod operation. So for instance when the value of phase along the blue curve reaches the lower bound zero, after taking the mod operation, the curve emerges in the upper region. To explain why the red and purple bifurcation curves disappear as α_1 increases beyond $\alpha_{ub}(k)$, again note from the 1-dimensional map shown in Fig. 3, that at large enough α_1, the unstable fixed point of that map disappears. This loss of existence corresponds to two fixed points disappearing in the 2-dimensional case. Similar arguments explain the bifurcation diagrams shown in panel (c)–(e).

Fixed points of the map can also be found by geometrically solving Eq. (14). Namely, in Fig. 6(a–b) we take a specific parameter set $k = 0.1, \alpha_1 = 0.08$ and show contour plots of the functions $F_1(x, y, k, \alpha_1) - x$ and $F_2(x, y, k, \alpha_1) - y$. The zero level curves are those that separate the blue and red regions and each constitute the x- and y-nullclines of (14). Plotting these nullclines on a common x–y plane, Fig. 6(c), the blue (red) curve corresponds to the x-(y)-nullcline. The four intersection points, A, B C and D are fixed points of the map. Based on numerical calculations of the eigenvalues at the linearization of the fixed points of the map (not shown), we conclude that point A is a stable node, points B and C are saddle points, and point D is an unstable node. Left unobserved are the manifolds associated with these fixed points. However, the contour plots and nullclines do reveal some information

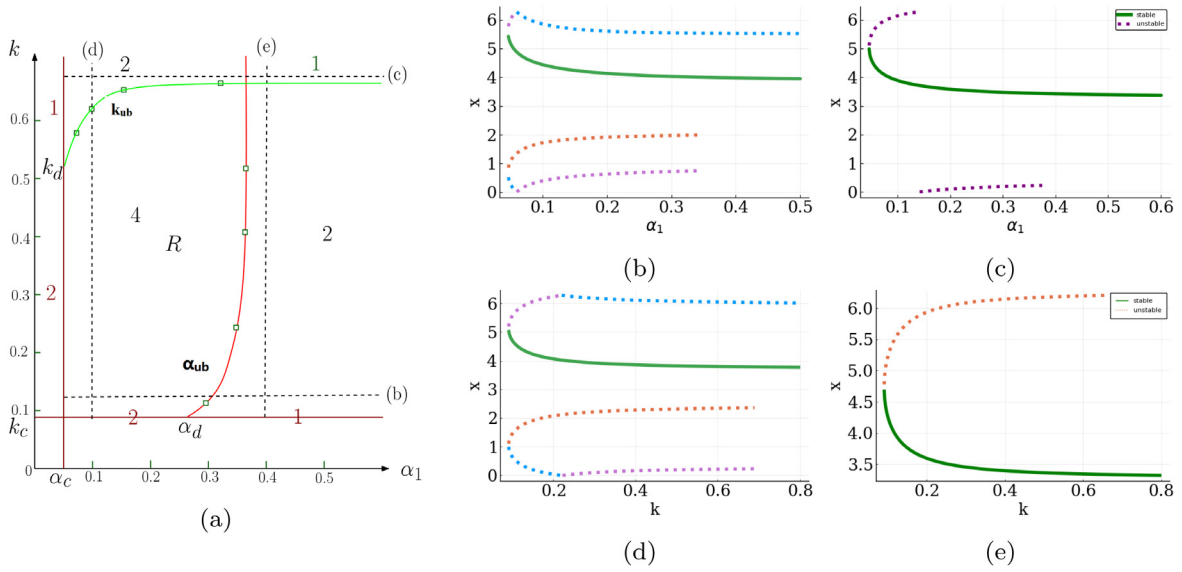

Fig. 5. Bifurcation diagrams regarding number of fixed points of the map: (a) The (α_1, k) parameter space showing how the number of fixed points depends on these parameters. There are no fixed points if either parameter lies below the critical value α_c or k_c. The region R is bounded by these lines and the curves $k_{ub}(\alpha_1)$ (green curve) and $\alpha_{ub}(k)$ (red curve). The number of fixed points in each regions is labeled. Squares along green and red curves represent parameter pairs that were tested during simulation. The rest of these curves were extrapolated. The dashed lines denote the parameter values we take for the 1-dimensional bifurcation curves shown in the other panels. (b) $k = 0.12$, increasing α_1, note that the dotted blue and purple curves switch location through 2π due to the mod operation, which is also seen in panel d. (c) $k = 0.65$, increasing α_1 and the transition from two to one fixed points. (d) $\alpha_1 = 0.1$, increasing k. (e) $\alpha_1 = 0.4$, increasing k and the transition from two to one fixed points.

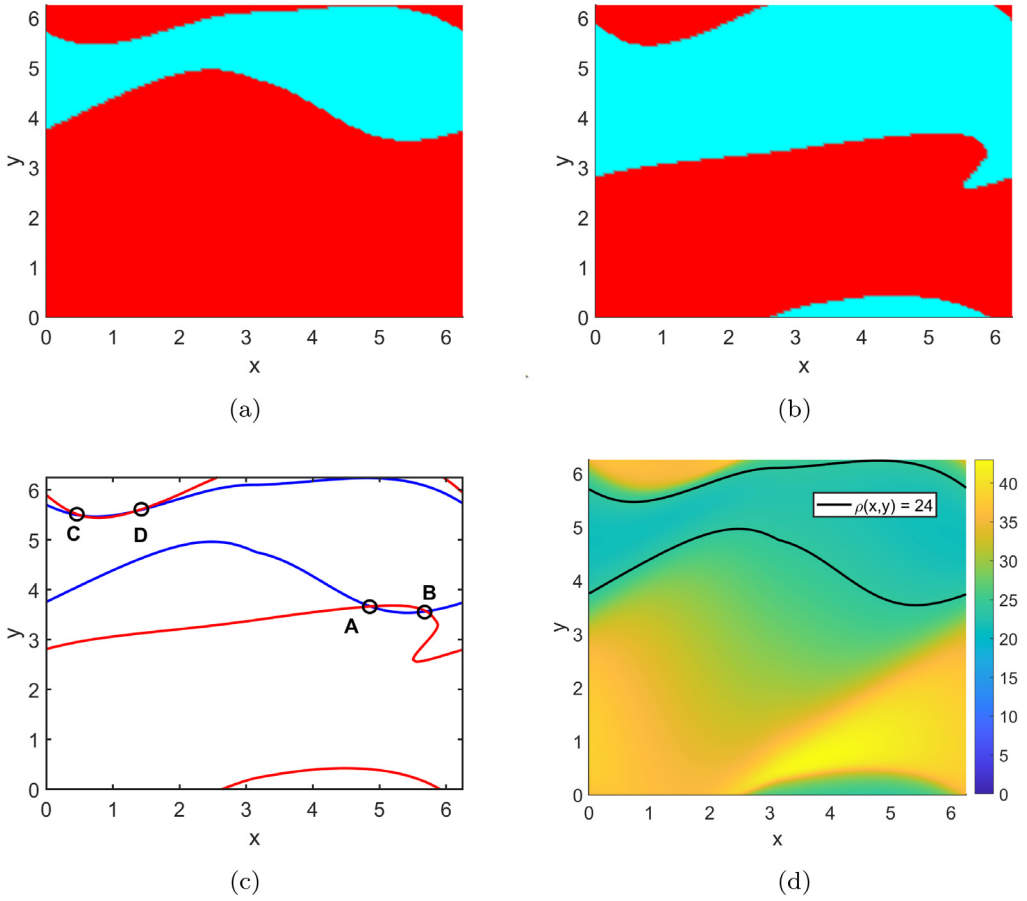

Fig. 6. (a) and (b): Contour plots of the map $F_1 - x$ and $F_2 - y$ at k=0.1, α_1=0.08. The curves separating the colors represent the contour curve of level 0. (c) Nullclines of the 2-dimensional map which correspond to the zero level curves of the contour plots (blue for (a) and red for (b)). The intersections of the nullclines are fixed points of the map and are labeled A–D. (d) Return time map $\rho(x, y)$ computed from direct simulations. The black curves represent where the return time is exactly 24 h. Note the similarities with panel (a).

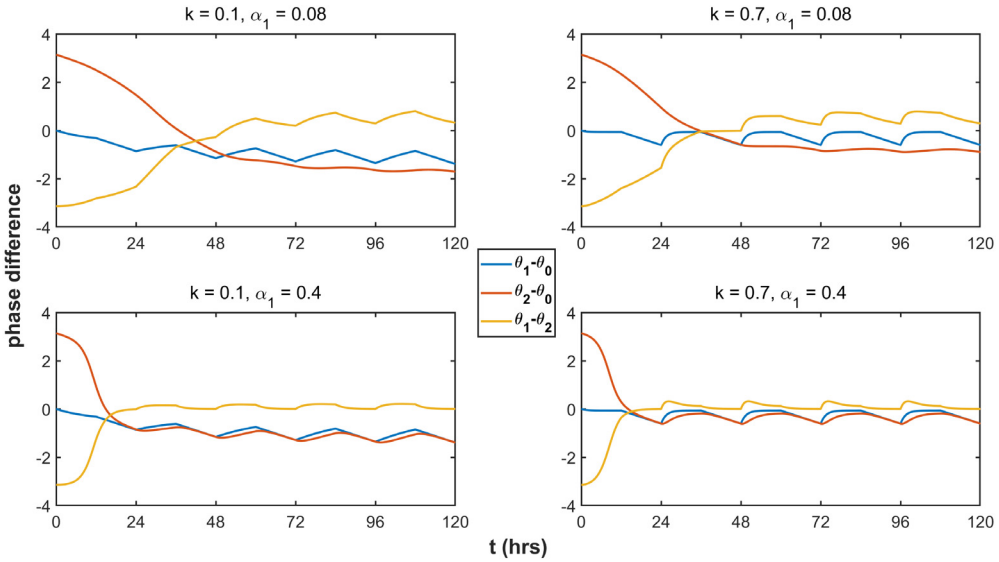

Fig. 7. Four parameter sets from different regions of the bifurcation space are shown. The relative phase difference between oscillators are plotted. For small k and α_1 (upper left), the oscillators take a few cycles to entrain. For large k, small α_1 (upper right), θ_1 entrains first (see blue curve). For large α_1, small k (lower left), θ_2 synchronizes to θ_1 first (see yellow curve). For both parameters large (lower right), both oscillators entrain quickly within the first 24 h cycle.

that will be useful for understanding the dynamics of the map. The region between the two blue curves where the level curves have a positive value corresponds to values for which the return time of θ_2 to the Poincare section $\mathcal{P}$ is less than 24 h. The complementary region therefore corresponds to values for which the return is greater than 24 h. In panel (d), we show the return time map $\rho(x, y)$ which allows us to also easily visualize its gradient, which will be useful in the section below where we locate the stable and unstable manifolds of the fixed points. Here notice that the return time map ρ is numerically computed by direct simulation of the three oscillator system. It agrees with the level curves in panel (a), which show, in a different way, the difference in the return time from 24 h calculated using the map.

3.4. Entrainment time

In Fig. 7, we have selected four different parameter sets to show how the entrainment time varies as a function of parameters, while starting from the same initial conditions. In the upper left panel, we plot the phase difference between oscillators for the parameter set from Case I used in Fig. 6. In the upper right panel, for Case II with a larger k value and small α_1 value, oscillator 1 entrains first to θ_0, as expected. In the lower left panel, the k value is the same as the first panel, but α_1 is now larger, also Case II. Now the two oscillators θ_1 and θ_2 synchronize first. In the lower right panel, where both k and α_1 are large, Case IV, all oscillators quickly entrain together. One other point to note in these panels is the phase difference at the entrained state. As would be expected, when the parameters k and/or α_1 are larger, the phase difference is smaller and the entrained state is more tightly synchronized.

We now use the map to compute the entrainment time. We shall investigate Cases I and II in some detail. Using the same parameter set as Fig. 6 $k = 0.1$, $\alpha_1 = 0.08$, we computed a heat map of entrainment times from different initial values; Fig. 8(a). The heat map is computed from a discretized initial condition space, by computing from the map how many iterates are needed from each initial condition to reach a neighborhood of the stable node A. Each iterate corresponds to a time, via the return map $\rho(v)$, which is then summed up to obtain the entrainment time. The longest entrainment times occur along the orange curves, while the shortest times occur along the dark blue ones. Noting that point A corresponds to a stable node, the results suggest that the dark blue curve corresponds to the strong stable manifold of this point. Note that this manifold also coincides with the 1-dimensional unstable manifold of the saddle point C. Since point B is a saddle, it will have a 1-dimensional stable manifold and that is what is depicted by the orange curve. This curve coincides with the weak unstable manifold of the unstable node D. If an initial condition were to begin on the stable manifold of either of these saddle points, then it would iterate in forward time to B and C and never entrain to the stable solution, i.e. it would have an infinitely long entrainment time. It follows, that points that lie close to these stable manifolds would accordingly have very long entrainment times before they eventually converge to the stable node at A. In the next section, we will further explore the manifold structure of the fixed points.

The heat map in Fig. 8(a) reveals important insights into how different initial configurations of the central and hierarchical oscillators lead to different entrainment times. The stable fixed point of that map occurs at roughly $x^* = 4.9$, $y^* = 3.65$. Note that changes in the initial x value correspond to changes in the LD phase with respect to the peripheral oscillator. Changes in the initial y value represent a desynchronization of oscillators 1 and 2 from their phase-locked relationship. Consider three different initial conditions: $x = 3.7$, $y = 3.65$ in which the LD phase is offset but the phase relationship between θ_1 and θ_2 is held constant; $x = 4.9$, $y = 2.7$ in which the LD phase is held constant but the phase relationship between θ_1 and θ_2 is perturbed; or $x = 3.7$, $y = 2.7$ in which the both the LD phase and the phase relationship between θ_1 and θ_2 are changed. The shortest reentrainment time is for the last case where oscillators 1 and 2 are desynchronized from one another while undergoing a shift in the LD phase. Here the initial condition $x = 3.7$, $y = 2.7$ lies near the (dark blue) strong stable manifold of stable node A for which iterates converge quickly and explains the fast reentraiment. Indeed any initial condition lying near the strong stable manifold of A will lead to fast reentrainment. Conversely, the longest reentrainment time is for the second case, where the oscillators are perturbed from their stable state but the LD phase does not change. Here the initial condition $x = 4.9$, $y = 2.7$ lies close the stable manifold of the saddle point B, which as mentioned above, leads to long reentrainment times. Note that if the change in LD phase is accompanied by a desynchronization of the peripheral and central oscillators that place the initial condition anywhere along the stable manifold of B, e.g. $x = 3$, $y = 1$, the reentrainment time will be very long. These results show that the manner in which a hierarchical system is perturbed from the phase-locked state is critical to determine how long reentrainment will occur.

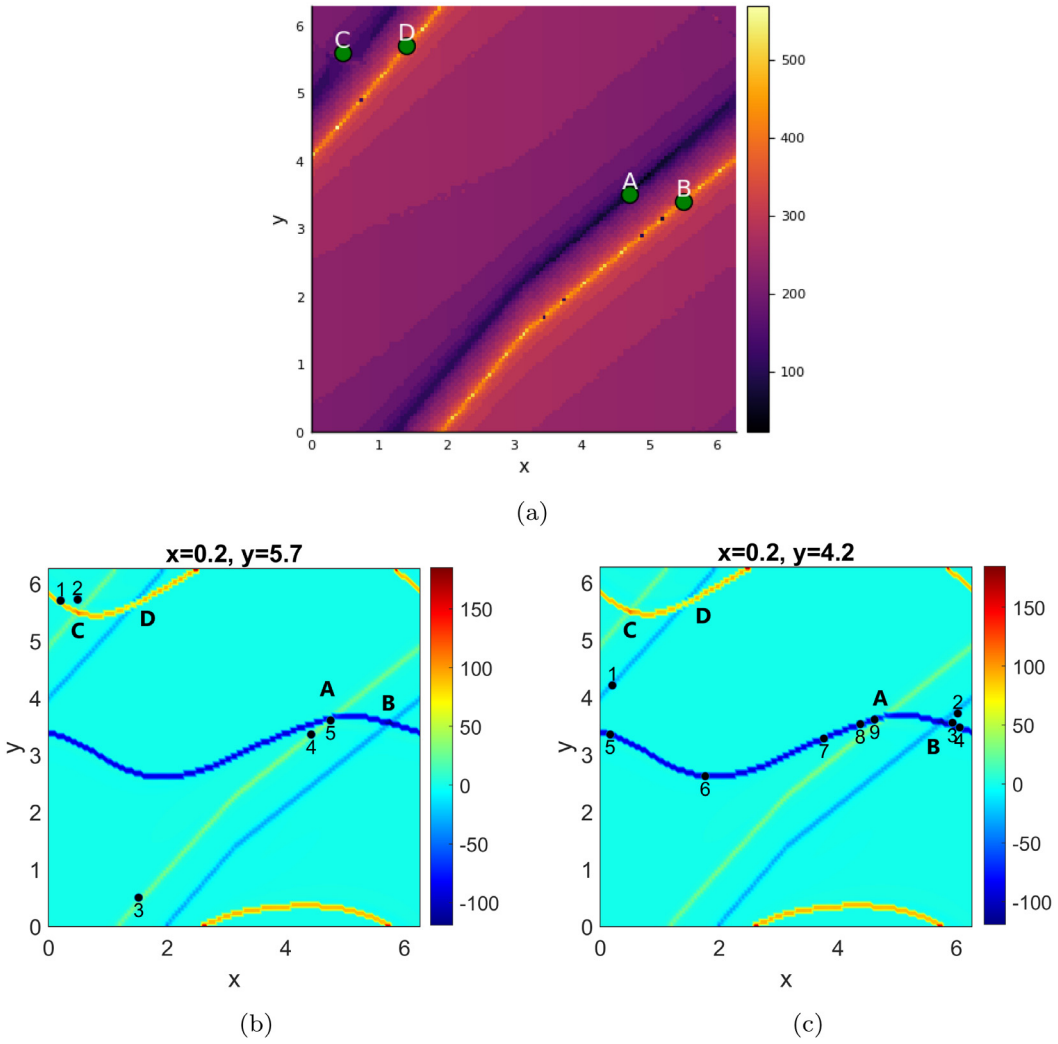

Fig. 8. (a) The heat map of the entrainment time. Point A is a stable node where the dark blue curve corresponds to the strong stable manifold of this point with the fastest entrainment time. This curve coincides with the unstable manifold of the saddle point C. Point B is a saddle, and its stable manifold is depicted by the orange curve indicating that points that lie close to it have the longest reentrainment times. This curve emanates from the unstable node D. (b–c) Fixed points occur at the intersection of the light yellow and blue (A), blue and light blue (B), light yellow and yellow (C) and light blue and yellow (D) curves. (b) Iterates from the initial condition $x = 0.2, y = 5.7$ near $W^s(C)$ are shown. The order of iterates and direction of entrainment is along the strong stable manifold of A which coincides with $W^u(C)$. The color map shows results from the Lagrangian descriptor method. (c) Iterates from the initial point $x = 0.2, y = 4.2$ near $W^s(B)$ are shown. The second through fourth iterates lie near B (labels overlap), but then wrap around the diagram and follow the weak stable manifold of A. The color map shows results from the Lagrangian descriptor method.

3.5. Entrainment direction

We applied the method of Lagrangian Descriptors [27], which is a numerical technique to find the stable and unstable manifolds of fixed points of flows and maps. Here we compute the sum of the arc length of five forward and five backwards iterates. We then take the difference of these values between nearby initial values to compute the gradient; see the Appendix for details of the method. At most points in phase space, the gradient will be close to zero (turquoise background in Fig. 8(b) and (c)) because there is not much difference in the arclength between nearby points. But between certain initial points, there are sharp changes in the arclength. These steep gradients reveal the stable and unstable manifolds of the fixed points. In Fig. 8(b) and (c), the light yellow curve represents $W^u(C)$, the unstable manifold of saddle point C, which coincides with the strong stable manifold of A; the light blue curve represents $W^s(B)$, the stable manifold of saddle point B, as well as the weak unstable manifold of D. The dark blue curve represents $W^u(B)$, the unstable manifold of B, which coincides with the weak stable manifold of A. The yellow curve represents $W^s(C)$, the stable manifold of C, which coincides with the strong unstable manifold of D.

To understand the direction of entrainment, we took two specific initial conditions to show how the iterates of the map become separated as a result of the manifold structure. In Fig. 8(b), we took an initial condition slightly above $W^s(C)$, the iterates move near $W^u(C)$ and converge quickly after just 5 iterates to the fixed point A. In this case, the x value of the map increases on the path to convergence, akin to a phase delay of the peripheral oscillator with respect to the LD phase. The phase of the central oscillator also phase delays (y increasing) to converge to its own stable phase. In Fig. 8(c), we took a point near $W^s(B)$, the iterates move near $W^s(B)$ for a few iterates, with x and y decreasing, until they are in a neighborhood of B. They then are attracted to the weak stable manifold of point A and phase delay in the x variable, but are not monotone in y. These kind of dynamics resemble reentrainment by partition as in [5]. From the second iterate onwards, the phase y for the central oscillator does remain close to its stable phase indicating that the central and peripheral oscillators are largely phase-locked while they entrain to the LD phase.

For minimizing reentrainment, what matters most is how close the initial value or one of its iterates lies to the strong stable manifold of the stable node A. When, as occurs in Fig. 8(b) for the second iterate, future iterates are constrained to lie near this manifold, iterates 3,

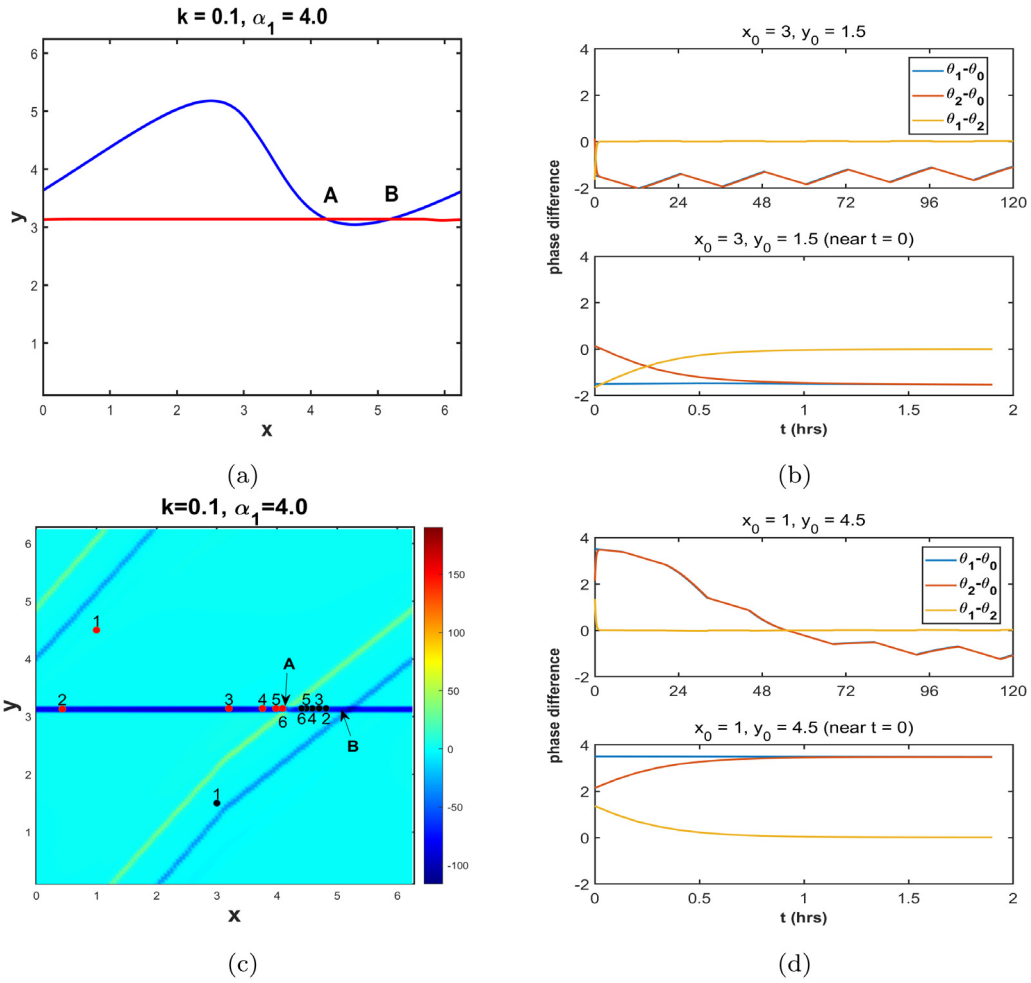

Fig. 9. Case II dynamics for $k = 0.1, \alpha_1 = 4$. (a) x-nullcline (blue) and y-nullclines (red) of the 2-dim map show two intersection points, A and B. (c) The Lagrangian Descriptors method reveals the stable and unstable manifolds of the fixed points. Fixed points A and B lie at the intersection of the blue curve with the light yellow and light blue curves, respectively. Iterates from two different initial conditions are shown; black dots: $x_0 = 3, y_0 = 1.5$; red dots: $x_0 = 1, y_0 = 4.5$. (b) and (d) The corresponding phase difference plot of the two initial condition in Fig. 9(c); note that the lower panels of (b) and (d) show the first two hours of the two initial conditions, to illustrate the rapid convergence of θ_2 to θ_1 as found near $t = 0$.

4 and 5, and thus converge quickly. Alternatively, in Fig. 8(c), the initial value lies close to the stable manifold of the saddle point B, meaning that future iterates transit near B before being attracted by the weak stable manifold A. What initially appears to be reentrainment through phase advance is blocked by the saddle structure of B, forcing the iterates to move in the opposite direction. From a mathematical view, this is somewhat surprising since stable and unstable manifolds of saddle points in maps do not necessarily provide a (local) separatrix structure for the phase space. This is unlike what can occur for stable and unstable manifolds for fixed points or periodic orbits of flows; see [10] for how this can occur in the context of circadian models.

Turning now to Case II of Fig. 5(a), we show analogous results when α_1 is large. In Fig. 9, we let $k = 0.1, \alpha_1 = 4$, so that oscillator 2 synchronizes to oscillator 1 quickly. For this case, there will be only two fixed points. In Fig. 9(a), we show the nullclines associated with Case II which intersect at two points; a stable node (A) and a saddle point (B). Note that the y-nullcline is horizontal at $y = \pi$. This is because oscillator 2 is slaved to oscillator 1. Thus when oscillator 2 is at the Poincaré section $\theta_2 = \pi$, oscillator 1 also lies there. Fig. 9(c) uses the Lagrangian Descriptor method to display the manifolds of the two fixed points. The light blue curve is the putative stable manifold of the saddle point. The blue curve is both the unstable manifold of the saddle point as well as the weak stable manifold of the stable node. The light yellow curve is the putative strong stable manifold of the stable node; see the Appendix for some additional comments about the caveat of "putative".

We have plotted six iterates starting from two distinct initial conditions $x_0 = 1$, $y_0 = 1.5$ (black dots) and $x_0 = 1$, $y_0 = 4.5$ (red dots). These iterates show very fast convergence towards the weak stable manifold of point A and then monotonic convergence in the x value towards A. This shows that after the first iterate, the direction of entrainment is primarily through phase delay (red dots) or advance (blue dots) for oscillator 1. In Fig. 9(b) and (d), we show the two representative phase differences, which show the quick convergence of oscillators 1 and 2, near $t = 0$ (lower panels of each) and the eventual entrainment of the pair through phase delay (b) or phase advance (d), as predicted by the map. Note here that we are plotting $\theta_1 - \theta_0$ and $\theta_2 - \theta_0$ so an increase in these values is a delay, and a decrease is an advance.

3.6. Generalization to $1 + N$ oscillators

We now return to study the full hierarchical system consisting of $1+N$ oscillators (2). As mentioned in the model section, we choose the Poincaré section to lie at $\theta_N = \pi$. This leads to an N-dimensional map for the phase of lights x, the phase of the central oscillator y and the phases of the other peripheral oscillators, z_i, $i = 2, \ldots, N-1$. We choose the values of k and α_i to lie within a parameter space that is equivalent to that of Case I of the $N = 2$ network. In particular, it is not hard to show that $\alpha_{i-1} \geq |\omega_0 - \omega_i|$ is a necessary condition for entrainment.

Using the work of the previous section, it is fairly straightforward to construct the following inductive argument. The one-dimensional

$N = 1$ entrainment map has two fixed points. The two-dimensional entrainment map has four fixed points. If the $N = k$ map has 2^k fixed points, then the $N = k + 1$ map has 2^{k+1} fixed points. Thus in the $1 + N$ dimensional system, there are 2^N fixed points. The stability of these fixed points can be determined inductively. At each deeper level of the hierarchy, each fixed point spawns two new ones, an unstable and stable one that inherit the existing stability properties from the higher level. For example, label the four fixed points of the $N = 2$ map as $2_{uu}, 2_{us}, 2_{su}$, and 2_{ss} with u and s corresponding to unstable and stable. The number of such symbols yields the dimension of the appropriate manifold of that fixed point. Then for the $N = 3$ map the eight fixed points would be labeled $3_{uuu}, 3_{uus}, 3_{usu}, 3_{uss}, 3_{suu}, 3_{sus}, 3_{ssu}$ and 3_{sss}. As is evident, only one of the fixed points is stable (that with only the s subscript), while the remaining fixed points are all unstable. Of those, one of them has eigenvalues that are all larger than one in absolute value (that with only the u subscript). The remaining unstable fixed points all possess both stable and unstable directions (i.e. higher dimensional saddle points). Regarding the direction of and time to entrainment, it is too difficult to fully categorize each of the possibilities. We note that based on our three-oscillator results, we conjecture that the fastest path to entrainment lies along the strong stable manifold of the stable fixed point. It is extremely difficult to give general conditions for the direction of entrainment since this depends critically on the initial position of each oscillator. Our results from the three-oscillator case suggest that the stable and unstable manifolds of the unstable fixed points will divide the phase space into regions where oscillators converge in different directions.

3.7. Application of the entrainment map to hierarchical models with mutually coupled peripheral oscillators

Having shown how to apply the entrainment map to hierarchical feed-forward networks, we now apply it to a model with multiple, mutually coupled peripheral oscillators. We will use the model of Kori et al. [24] who studied a network with one central and two peripheral oscillators and used an order parameter to reduce the phase of the peripheral oscillators to an averaged phase oscillator. The goal here is to determine if desynchronizing (phase tumbling) the peripheral oscillators at the moment of the LD phase shift leads to faster reentrainment. Eq. (3) describes the system. Note that each peripheral oscillator couples to the others and is assumed to be symmetric, $\alpha_2 = \alpha_3$. The averaged phase $\bar{\theta}(t)$ is defined by

$$Re^{i\bar{\theta}} = \frac{1}{2}(e^{i\theta_2} + e^{i\theta_3}), \tag{17}$$

where $R(t)$ is the synchronization level; when the value of R is at extremes, 1 and 0, the oscillators are either completely in-phase or are π degrees out of phase. Kori et al. [24] showed that

$$R(t) = |\cos\frac{\Delta\theta(t)}{2}|, \tag{18}$$

where $\Delta\theta(t) = \theta_2(t) - \theta_3(t)$. Notice that $R(t)$ is a function of t. The phase difference of θ_2 and θ_3 changes over time but does become 2π-periodic with small amplitude about its mean as the solution entrains. We fix the R value to a value near the mean of this steady state of $R(t)$ to define the averaged system. The new model that we consider is given by

$$\begin{aligned}
\frac{d\theta_0}{dt} &= \omega_0 \\
\frac{d\theta_1}{dt} &= \omega_1 + kf(\theta_0)\sin(\theta_0 - \theta_1) \\
\frac{d\bar{\theta}}{dt} &= \bar{\omega} + \alpha R\sin(\theta_1 - \bar{\theta}).
\end{aligned} \tag{19}$$

The parameters that were not previously defined are $\bar{\omega} = 2\pi/29, k = 0.08, \alpha = 0.1, R = 0.88$. The k value is chosen based on the results from the last section so that the central oscillator is entrained. The order parameter value for R is chosen to be in a neighborhood of the mean R value obtained from simulation for the entrained solution of the full set of Eqs. (3). The two-dimensional entrainment map is built now by placing the Poincaré section on the central oscillator at $\theta_1 = \pi$. The variable x continues to represent the phase of light and y now represents the phase of the averaged oscillator.

In Fig. 10(a), we plot the nullclines where blue represents x-nullcline, red represents y-nullcline. The x-nullclines are now vertical since the Poincaré section is taken on the central oscillator thus decoupling the light phase from any dependence on the averaged oscillator. Intersections of the nullclines, as before, correspond to fixed points of the entrainment map. The stable fixed point is labeled A, the two saddles points are B and C and the unstable node is point D. Fig. 10(b) shows the entrainment time required for each initial condition. There is very little dependence on y for this choice of parameters, indicating that the entrainment of the central oscillator to the light-dark forcing governs entrainment times. Fig. 10(c) shows the results of the Lagrangian Descriptor method which clearly reveals the structure of the manifolds of the fixed points. Notice here that the color is slightly different than in previous figures (green means zero gradient). The phase differences for the full model (3) and the averaged model (19) are shown in Fig. 10(d). The top panel shows that for the chosen parameters, θ_1 and θ_3 entrain to LD cycle through phase advance (the curves decrease), while the other peripheral oscillator, θ_2 entrains initially through phase advance followed by phase delay. By comparison, the phase difference of the averaged phase equation (lower panel) captures only some of the dynamic behavior of the system.

We now turn our attention to the question of whether desynchronization of the peripheral oscillators affects their reentrainment times after an abrupt change in the light-dark phasing. An et al. [21] suggest that desynchronization of oscillators at the time of shift in the light phasing can speed up their ultimate reentrainment. Kori et al. [24], alternatively, suggest the opposite. Indeed they suggest that the evolution of the order parameter R value from the desynchronized levels, e.g. close to 0, towards its ultimate mean steady state value will lead to slower reentrainment since the effect of the central oscillator will have opposing effects on the peripheral oscillator. The basis for the Kori et al. claim is that the rate at which the average oscillator entrains is proportional to R (see Eq. (8) in their paper). Thus smaller values of R lead to slower reentrainment. We show here that in some sense both are partially correct. In fact, we will show that the level of synchrony of the peripheral oscillators in the stable entrained solution seems to determine the efficacy of phase tumbling. In particular, when R is close to one, phase tumbling does not seem to affect reentrainment times over a range of light onset phases. When R is smaller, then phase tumbling can either speed up or slow down the reentrainment.

To assess this, we computed how quickly the order parameter as a function of time $R(t)$ approaches its mean steady state value. Fig. 11(a, c) shows two different cases, $R \approx 0.88$ and $R \approx 0.74$. In both simulations we started one simulation with oscillators 2 and 3 completely synchronized (solid blue), $R_0 = 1$, and another simulation with the oscillators maximally separated by, $\theta_2(0) = \theta_3(0) + \pi$ (red dashed), $R_0 = 0$ with the light phase at $x = 0$. As is evident, the order parameter evolves in different ways for each of the cases, but there is not much qualitative differences in the time in which the $R_0 = 0$ and $R_0 = 1$ time courses reach a neighborhood of the mean R value for each case. So the actual initial synchronization level at $t = 0$ may not meaningfully affect synchronization time. What is true is that for the smaller R value, panel (c), the time in hours to reach this steady state is longer (by about two days), which is consistent with the claim of Kori et al. However the convergence to the mean R value is not the same as entrainment. In Fig. 11(b, d), we plot the reentrainment times over a range of different initial R_0 values (0, 0.35, 0.7, 1.0) for a range of different phase shifts of light onset shown by different values from 0 to 24 on the horizontal axis. Note from panel (b) that when the ultimate entrained solution is itself fairly well synchronized, $R \approx 0.88$, the initial synchrony value R_0 plays no role in determining the reentrainment time. Indeed the interpolated curves nearly overlap one another. This shows that

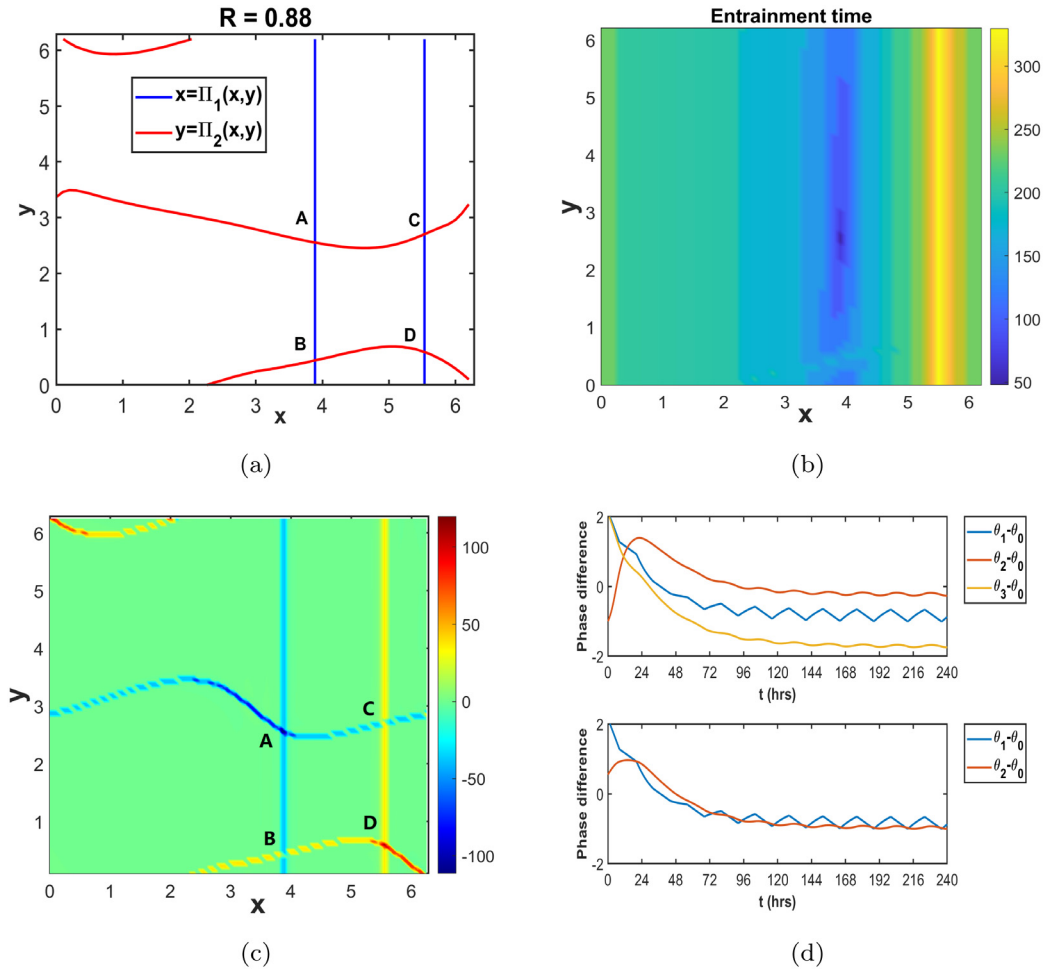

Fig. 10. Entrainment map for the averaged oscillator model: (a) The x-nullcline (blue) and y-nullcline (red) of the entrainment map intersect at four fixed points labeled A–D. (b) Entrainment time required for each initial condition. (c) The Lagrangian Descriptor method which plots the gradient of the arclength for iterations for each initial condition uncovers the manifolds of the various fixed points. The strong stable and unstable manifolds of fixed points A and D are independent of the averaged oscillator phase since the Poincaré section lies at $\theta_1 = \pi$. (d) The phase difference between oscillators of the original model and the averaged model; see text for more details.

phase tumbling has little effect in changing reentrainment times for this case. Alternatively, panel (d) shows that when the entrained solution displays a greater phase difference between the peripheral oscillators, then R_0 and the initial phase of the light determine the reentrainment time. Thus phase tumbling here has an effect on entrainment times. However, there is little, to no predictability of whether phase tumbling, i.e. starting with small R_0, will decrease reentrainment times. There are certainly cases where it does, consistent with An et al. but it is appears to be highly dependent on the initial phasing of the light onset.

4. Discussion

In this paper, we established a mathematical basis through which to understand the entrainment of circadian oscillators in a few different hierarchical systems. We utilized the well known and widely applicable Kuramoto model [18] to consider a relatively low-dimensional phase space. Generalizing from previous work [15,16], we were able to derive an N-dimensional entrainment map for a feed-forward hierarchical network, which we then analyzed in detail for the case $N = 2$. Fixed points of the map correspond to stable and unstable periodic solutions of the original equations. Importantly, we showed how the stable and unstable manifolds of the fixed points organized the iterates of the map leading to a clearer understanding of the time to and direction of reentrainment of oscillators after an abrupt change in the light-dark phasing in the network. We also derived a two-dimensional entrainment map for a system consisting of a central and two mutually coupled peripheral oscillators. There we analyzed the time to entrainment as a function of the initial and final levels of synchrony of the peripheral oscillators. We showed that desynchronized initial conditions can lead to faster reentrainment, but only for specific switches of the light onset phase and only when the peripheral oscillators in the stable phase-locked solution are not too tightly synchronized.

We demonstrated that the fixed points of the entrainment map correspond to different types of phase-locked solutions of the circadian system. For $N = 2$ and parameter values in which there are four fixed points, the stable fixed point represents the solution in which the central and peripheral oscillators are entrained to the light-dark forcing, the two saddle-points represent solutions where one of the two oscillators is entrained but the other is in an unstable state. and the unstable node where both are in an unstable periodic state. In turn, the stable and unstable manifolds of the saddles organize the convergence of iterates to the stable entrained solution. That the manifolds of the map guide the direction of entrainment, on one hand, is somewhat surprising given that the manifolds of a map, in general, do not separate phase space in the way they can for flows. However, for the case of entrainment of a single central oscillator, Creaser et al. [10] have shown via simulation and bifurcation continuation methods that the stable and unstable manifolds of the limit cycle solutions of a two-dimensional model do guide the direction of entrainment. Thus we expect that this is also the case for the lower dimensional phase-based models. Given, earlier findings of Bordyugov et al. [20] that reduced phase models can accurately mimic more complex biochemical

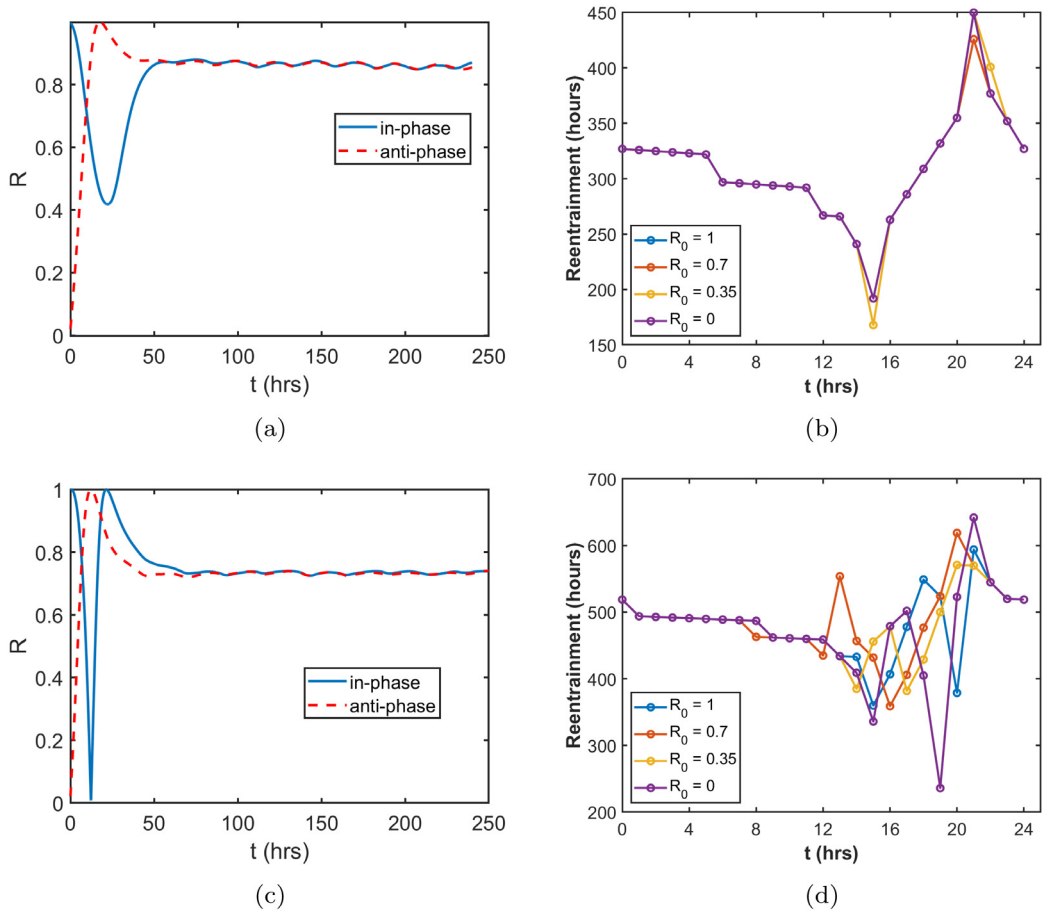

Fig. 11. (a) The evolution of synchronization level of two specific simulations with $R \approx 0.88$ (anti-phase and in-phase initial conditions shown in dashed red in solid blue, respectively) show similar convergence times. (b) For four different initial R_0 values, the reentrainment times with different initial phase of light onset shown here by different values along the horizontal axis given in hours. (c) For another stable value $R \approx 0.74$, where we increased the heterogeneity of the peripheral oscillators by changing $\omega_2 = \frac{2\pi+2.4}{29}$ and $\omega_3 = \frac{2\pi-2.4}{29}$, the anti-phase solution has faster convergence. (d) Similar to panel (b) in set up. Here desynchronization of the peripheral oscillators shortens the reentrainment but only for a range of light shifts.

modes, our findings indicate that there may be some general principle underlying the dynamics of feed-forward hierarchical circadian systems regardless of the model equations being used. Namely, for each entrained solution or unstable periodic solution, as a new oscillator is added to the chain in the hierarchy, two new solutions arise, one that is stable and another that is unstable with respect to the phase-locked state at the higher level that spawned them. Thus a system of N coupled oscillators can exhibit parameter regimes in which 2^N periodic solutions exist, with only one being stable. All other solutions display some form of instability, $2^N - 2$ being of saddle type, and a lone fixed point that is an unstable node. The results found here are also consistent with earlier numerical findings of Leise and Siegelmann [5] whose work showed that peripheral oscillators need not entrain in the same direction as central ones. As we show in Fig. 8 there can be considerable variation in how these oscillators entrain based on their initial states. In some cases, the entrainment can systematically be categorized as phase advancing or phase delaying. But in other cases, different oscillators in the network can entrain through some combination of directions.

One goal of the work was to clarify whether phase tumbling of peripheral oscillators [21–23] leads to faster entrainment. Using a combination of the order parameter formulation applied to the entrainment map together with simulations of the full mutually coupled network, we showed that for the Kuramoto model, no definite answer can be provided. Depending on parameters, initial conditions and the phase of light onset, phase tumbling may speed up, slow down or have no effect on reentrainment times. We could not find a systematic way to predict when phase tumbling would be beneficial. This may be due to the one-dimensional nature of the intrinsic phase space of each Kuramoto oscillator. Trajectories have very limited ability to deviate in phase space unlike what might occur if higher dimensional and more complicated circadian oscillators are considered. Indeed, using a Poincaré oscillator, which models both the amplitude and phase of oscillations may be more relevant. This is of particular interest given the recent findings of Jeong et al. [7] who show in experiment and with biochemical modeling that strong oscillators that receive direct LD input can display fast reentrainment despite having large amplitude oscillations. They argue that strong oscillators have high sensitivity to light meaning that groups of strong oscillators naturally desynchronize, leading to phase tumbling for which there is fast reentrainment. It would be of interest to see if a reduced phase–amplitude model can capture this behavior and whether the structure of the invariant manifolds of the phase space continue to guide the reentrainment process.

Declaration of competing interest

The authors declare that they have no known competing financial interests or personal relationships that could have appeared to influence the work reported in this paper.

Acknowledgments

The work of Guangyuan Liao was supported by the National Natural Science Foundation of China (Grant No. 11901073), Science and technology research project of Chongqing Education Commission, China (Grant No. KJQN201900619) and the Scientific Research Starting Foundation of Chongqing University of Posts and Telecommunications, China (Grant No. A2022-289). The authors thank Casey Diekman for helpful discussions.

Appendix A. Derivation of Eq. (15)

From the first of Eq. (14), a necessary condition for entrainment is $\rho(x, y, k, \alpha_1) = 24$. Substituting into Eq. (12), and simplifying yields,

$$\int_0^{24} \sin\left(\theta_1(s) - \theta_2(s)\right) ds = \frac{2\pi - 24\omega_2}{\alpha_1}. \tag{A.1}$$

From the Mean Value Theorem for integrals, there exists a $s_1 \in [0, 24]$, such that

$$\sin\left(\theta_1(s_1) - \theta_2(s_1)\right) = \frac{2\pi - 24\omega_2}{24\alpha_1} = \frac{\omega_0 - \omega_2}{\alpha_1} \tag{A.2}$$

Simplify the second equation of (14) to obtain

$$\int_0^{24} f(\theta_0(s)) \sin\left(\theta_0(s) - \theta_1(s)\right) ds = \frac{2\pi - 24\omega_1}{k}. \tag{A.3}$$

Notice that, $\theta_0(s) = x + \omega_0 s$, so we apply a change of variable $u = x + \omega_0 s$, to obtain

$$\int_x^{x+2\pi} f(u) \sin\left(\hat{\theta}_0(u) - \hat{\theta}_1(u)\right) du = \omega_0 \frac{2\pi - 24\omega_1}{k}, \tag{A.4}$$

where $\hat{\theta}_i(u) = \theta_i(\frac{u-x}{\omega_0}), i = 0, 1$. If $x > \pi$, then the integral is only nonzero during the interval $[2\pi, 3\pi]$,

$$\int_{2\pi}^{3\pi} \sin\left(\hat{\theta}_0(u) - \hat{\theta}_1(u)\right) du = \omega_0 \frac{2\pi - 24\omega_1}{k} \tag{A.5}$$

If $x < \pi$, the integral has two nonzero parts.

$$\left(\int_x^{\pi} + \int_{2\pi}^{x+2\pi}\right) \sin\left(\hat{\theta}_0(u) - \hat{\theta}_1(u)\right) du = \omega_0 \frac{2\pi - 24\omega_1}{k} \tag{A.6}$$

Using the periodicity of sine function, we can shift the second integral by 2π,

$$\begin{aligned} \left(\int_x^{\pi} + \int_0^{x}\right) \sin\left(\hat{\theta}_0(u) - \hat{\theta}_1(u)\right) du &= \omega_0 \frac{2\pi - 24\omega_1}{k} \\ \int_0^{\pi} \sin\left(\hat{\theta}_0(u) - \hat{\theta}_1(u)\right) du &= \omega_0 \frac{2\pi - 24\omega_1}{k} \\ \sin\left(\theta_0(s_2) - \theta_1(s_2)\right) &= \frac{2(\omega_0 - \omega_1)}{k}, \end{aligned} \tag{A.7}$$

where the second equality is equivalent to Eq. (A.5), the last equality again uses the Mean Value Theorem and we change $\hat{\theta}$ back to θ.

Appendix B. The Lagrangian descriptor method

The Lagrangian descriptor method was first introduced in [27]. This tool is able to provide a global dynamical picture, including a method to visualize the geometric structures associated with stable and unstable manifolds for arbitrary flows and maps. Additionally, the implementation is relatively simple compared to other methods. There are other construction methods such as Search Circle [28] and growing method [29] for finding invariant manifolds. However, the implementation of these methods is not as easy as the Lagrangian descriptor method for the current context and are thus less suitable.

Consider the map defined by $x \mapsto F(x), x \in \mathbb{R}^n$. Similarly to [30], we define the Lagrangian descriptor by considering an orbit $\{x_i\}_{i=-N}^{N}$, with $x_0 = y$ over N forward or backward iterates; here we are using generic variables x and y, which have distinct meaning from their use in main part of the manuscript. The Lagrangian descriptor function is defined by

$$M(y, N) = \sum_{i=-N}^{N-1} \|x_{i+1} - x_i\|. \tag{B.1}$$

To understand why $M(y, \tau)$ is useful for revealing the geometric structures of the vector field, consider two initial conditions y_1, y_2 in that phase space. If y_1, y_2 are close enough, then $M(y_1, \tau)$ and $M(y_2, \tau)$ should be too, at least for a small number of iterates. But this is not true when we choose two points in different dynamical regions of the vector field. For example, for two regions separated by a stable manifold of an unstable fixed point. $M(y, \tau)$ will have a qualitative difference on the boundary. Hence, the derivative of M along these boundaries is discontinuous. Thus the sharp changes in properties of $M(y, t)$ reveal the stable manifold of the fixed point.

Turning now to Fig. 9(c), the Lagrangian descriptor method reveals where there are large gradients in M, which we have associated with the stable and unstable manifolds of points A and B. However, the direction of movement of iterates along these putative manifolds is not consistent. Consider the stable manifold of saddle point B (light blue curve). Iterates in the right portion of the graph move towards B. Because of periodicity of the domain, the iterates on this curve near the left boundary should point left and down, while those on the top boundary should point up and right. This is inconsistent with this curve being the stable manifold of B. Instead we conjecture that there is an additional structure in the space that is acting as a separatrix forcing iterates to move in different directions. Perhaps the methods of Creaser et al. [10] extended to maps may be able to resolve this issue.

References

[1] D. Bell-Pedersen, V.M. Cassone, D.J. Earnest, S.S. Golden, P.E. Hardin, T.L. Thomas, M.J. Zoran, Circadian rhythms from multiple oscillators: Lessons from diverse organisms, Nature Rev. Genet. 6 (7) (2005) 544–556.

[2] M.C. Antle, R. Silver, Orchestrating time: Arrangements of the brain circadian clock, Trends Neurosci. 28 (3) (2005) 145–151.

[3] A.-M. Finger, C. Dibner, A. Kramer, Coupled network of the circadian clocks: A driving force of rhythmic physiology, FEBS Lett. 594 (17) (2020) 2734–2769.

[4] F. Damiola, N. Le Minh, N. Preitner, B. Kornmann, F. Fleury-Olela, U. Schibler, Restricted feeding uncouples circadian oscillators in peripheral tissues from the central pacemaker in the suprachiasmatic nucleus, Genes. Dev. 14 (23) (2000) 2950–2961.

[5] T. Leise, H. Siegelmann, Dynamics of a multistage circadian system, J. Biol. Rhythms 21 (2006) 314–323.

[6] U. Abraham, A.E. Granada, P.O. Westermark, M. Heine, A. Kramer, H. Herzel, Coupling governs entrainment range of circadian clocks, Mol. Syst. Biol. 6 (1) (2010) 438.

[7] E.M. Jeong, M. Kwon, E. Cho, S.H. Lee, H. Kim, E.Y. Kim, J.K. Kim, Systematic modeling-driven experiments identify distinct molecular clockworks underlying hierarchically organized pacemaker neurons, Proc. Natl. Acad. Sci. 119 (8) (2022) e2113403119.

[8] Z. Lu, K. Klein-Cardeña, S. Lee, T.M. Antonsen, M. Girvan, E. Ott, Resynchronization of circadian oscillators and the east-west asymmetry of jet-lag, Chaos 26 (9) (2016) 094811.

[9] C.O. Diekman, A. Bose, Reentrainment of the circadian pacemaker during jet lag: East-west asymmetry and the effects of north-south travel, J. Theoret. Biol. 437 (2018) 261–285.

[10] J.L. Creaser, C.O. Diekman, K.C.A. Wedgwood, Entrainment dynamics organised by global manifolds in a circadian pacemaker model, Front. Appl. Math. Stat. (2021) 52.

[11] C.O. Diekman, A. Bose, Beyond the limits of circadian entrainment: Non-24-h sleep-wake disorder, shift work, and social jet lag, J. Theoret. Biol. 545 (2022) 111148.

[12] T. Kapitaniak, Transition to hyperchaos in chaotically forced coupled oscillators, Phys. Rev. E 47 (1993) R2975–R2978.

[13] N. Kopell, G.B. Ermentrout, T.L. Williams, On chains of oscillators forced at one end, SIAM J. Appl. Math. 51 (5) (1991) 1397–1417.

[14] B. Pfeuty, Q. Thommen, M. Lefranc, Robust entrainment of circadian oscillators requires specific phase response curves, Biophys. J. 100 (11) (2011) 2557–2565.

[15] C.O. Diekman, A. Bose, Entrainment maps: A new tool for understanding properties of circadian oscillator models, J. Biol. Rhythms 31 (6) (2016) 598–616.

[16] G. Liao, C. Diekman, A. Bose, Entrainment dynamics of forced hierarchical circadian systems revealed by 2-dimensional maps, SIAM J. Appl. Dyn. Syst. 19 (3) (2020) 2135–2161.
[17] B. Novák, J.J. Tyson, Design principles of biochemical oscillators, Nature Rev. Mol. Cell Biol. 9 (12) (2008) 981.
[18] Y. Kuramoto, Chemical Oscillations, Waves, and Turbulence, Springer, Heidelberg, Germany, 1984.
[19] A. Granada, H. Herzel, How to achieve fast entrainment? The timescale to syncrhonization, PLoS One 4 (9) (2009) e7057.
[20] G. Bordyugov, U. Abraham, A. Granada, P. Rose, K. Imkeller, A. Kramer, H. Herzel, Tuning the phase of circadian entrainment, J. Royal Soc. Interface 12 (108) (2015) 20150282.
[21] S. An, R. Harang, K. Meeker, D. Granados-Fuentes, C.A. Tsai, C. Mazuski, J. Kim, F.J. Doyle, L.R. Petzold, E.D. Herzog, A neuropeptide speeds circadian entrainment by reducing intercellular synchrony, Proc. Natl. Acad. Sci. 110 (46) (2013) E4355–E4361.
[22] L. Roberts, T.L. Leise, T. Noguchi, A.M. Galschiodt, J.H. Houl, D.K. Welsh, T.C. Holmes, Light evokes rapid circadian network oscillator desynchrony followed by gradual phase retuning of synchrony, Curr. Biol. 25 (7) (2015) 858–867.
[23] C. Mazuski, E.D. Herzog, Circadian rhythms: To sync or not to sync, Curr. Biol. 25 (8) (2015) R337–R339.
[24] H. Kori, Y. Yamaguchi, H. Okamura, Accelerating recovery from jet lag: Prediction from a multi-oscillator model and its experimental confirmation in model animals, Sci. Rep. 7 (2017) 46702.
[25] C.J. Morris, T.E. Purvis, J. Mistretta, F.A.J.L. Scheer, Effects of the internal circadian system and circadian misalignment on glucose tolerance in chronic shift workers, J. Clin. Endocrinol. Metab. 101 (3) (2016) 1066–1074.
[26] K. Serkh, D.B. Forger, Optimal schedules of light exposure for rapidly correcting circadian misalignment, PLoS Comput. Biol. 10 (4) (2014) e1003523.
[27] A.M. Mancho, S. Wiggins, J. Curbelo, C. Mendoza, Lagrangian descriptors: A method for revealing phase space structures of general time dependent dynamical systems, Commun. Nonlinear Sci. Numer. Simul. 18 (12) (2013) 3530–3557.
[28] J.P. England, B. Krauskopf, H.M. Osinga, Computing one-dimensional stable manifolds and stable sets of planar maps without the inverse, SIAM J. Appl. Dyn. Syst. 3 (2) (2004) 161–190.
[29] B. Krauskopf, H. Osinga, Growing 1D and quasi-2D unstable manifolds of maps, J. Comput. Phys. 146 (1) (1998) 404–419.
[30] C. Lopesino, F. Balibrea, S. Wiggins, A.M. Mancho, Lagrangian descriptors for two dimensional, area preserving, autonomous and nonautonomous maps, Commun. Nonlinear Sci. Numer. Simul. 27 (1–3) (2015) 40–51.